

The Compton Effect and GRB Polarimetry

PH 587: B. Tech Project

by

Yashowardhan Rai (22b2132)

Under the guidance of

Prof. Varun Bhalerao



Department of Physics
Indian Institute of Technology, Bombay
Mumbai 400 076

Contents

1	Introduction	4
1.1	A primer on Gamma Ray Bursts	4
1.2	Theory of polarisation	6
1.2.1	Stokes' Parameters	6
1.3	The Poincare Sphere	7
1.3.1	Micro-polarisation to macro-polarisation	7
1.4	Importance of Polarization to GRBs	10
2	Detecting x-rays and γ-rays	11
2.1	The Compton Effect	12
2.2	The Klein-Nishina Cross Section	12
2.3	The Modulation Curve	13
2.4	Relevant Detection Principles	15
3	GRB Compton Polarimetry	16
3.1	State of GRB Polarimetry	16
3.2	Compton Double Counting in Practice	17
3.2.1	Role of Geant4 simulations for CZTI	18
3.2.2	Kinematic and Energetic Criteria	18
3.3	Building the Modulation Curve	19
3.4	Comparison of AstroSat-CZTI and POLAR	21
4	Monte-Carlo Model and Results of Simulations	22
4.1	Assumptions and Scope of the Model	22
4.2	Histograms of Mono-energetic simulations	24
4.2.1	Oblique incidences	27
4.3	Daksha : Improving upon CZTI	31
5	Conclusion and Future work	33
5.1	Joint Polarisation Measurements	33
5.2	10 year catalog of AstroSat CZTI	34
5.3	Daksha : Next generation Polarisation mission	34
5.4	Acknowledgments	34

List of Figures

1.1	Comparison Energy Spectrum of Band and Synchrotron	5
1.2	Comparison of Energy flux spectrum of Band and Synchrotron	5
1.3	Visualisation of polarised Synchrotron radiation by Emma Alexander . .	6
1.4	Visualisation of Stokes' Parameters by Emma Alexander	7
1.5	The Poincare Sphere	8
1.6	Synchrotron Emission with Toroidal field ^[6]	9
1.7	Red - SO model, Green - SR model, Blue - Compton Drag model	10
2.1	Figure showing dominant process for various Z and $h\nu^{[8]}$	11
2.2	Schematic description of classical scattering	13
2.3	Analytical Heat Map for $E = 200\text{keV}$	14
2.4	Visualisation of Compton Scattering within the POLAR detector ^[9]	14
3.1	Histogram of time intervals between events for a CZT detector [4]	17
3.2	Actual Photo of the AstroSat CZTI	18
3.3	Overlaid Polarised and Unpolarised runs	20
4.1	Scattering obtained using rejection sampling of $P(\theta, \phi)$	23
4.2	Earlier 200 keV map for reference	23
4.3	Unpolarised raw histograms	24
4.4	Initial, raw histograms, for $Y=X$ and X axis polarisation	25
4.5	Geometry corrected counts for X axis and $Y=X$ polarisation	26
4.6	Results of curve fitting on X axis polarised	26
4.7	Results of curve fitting on X axis polarised	27
4.8	Geometry of the 3x3 detector	28
4.9	Vectors involved in rotation	29
4.10	Scattering distribution for unpolarised 30 degree incidence	29
4.11	Distribution of 100% polarised fraction for oblique incidence	30
4.12	Overplotted variations of the best fit curve	30
4.13	A simulation with $\theta = 45$	31
4.14	Schematic of Daksha	32

Abstract

The Compton Effect is an important interaction high energy photons have with matter and has a wide range of uses when it comes to dealing with X-ray and Gamma-ray astronomy. The relevant aspect here is the polarisation dependence of the scattering cross section with polarisation angle. Namely the scattering cross section peaks at azimuthal angles perpendicular to the polarisation. This fact is exploited by many space instruments such as AstroSat-CZTI and POLAR, when analysing Gamma-Ray Bursts (GRBs). The resulting modulation curves and comparisons with the Geant4 simulations of similarly located events allow us to deduce the polarisation fraction and polarisation angle of the bursts which has profound implications on the theory of GRBs as a whole. In this report, I endeavour to explain the operating principle behind the usage of the AstroSat-CZTI as a polarimeter, present results of a simplified python-based Monte Carlo simulation of the same and explain the significance to such measurements to the study of GRBs.

Chapter 1

Introduction

To a great extent, our understanding of physical laws are limited by the physical processes that commonly occur on earth, and the common energy ranges that we as medium-sized organisms have access to. However in order to explain the irregularities we have come across, we have built up our grandest and most all encompassing theories (General Relativity, Quantum Field Theory etc.) and to test these theories we require extremely abnormal conditions, such as high velocities, densities and temperatures.

One common methodology has do with characterising the nano-scale by observing the scattering of high energy particles colliding with each other. Much has been done in this vein and great progress has been made. Yet we are limited by how large of a collider we can construct and install. Good thing the universe is not constrained the same as us when deciding how the cosmos evolves with time. Ever since the middle ages, great progress has been made in physics by observing the motion of planets and now, with our superior telescopes and probes we started observing much further away objects. With that, and the discovery of atomic theory and radiation, it became increasingly clear that we are being bathed with multitudes of types of particles and space is not as empty as we thought. Fast forward to the present, the detection and characterisation of high and low energy radiation from outer space now involves incredible engineering and even better interpretation using statistics and software some of which I aim to talk about in the context of GRB Polarimetry.

1.1 A primer on Gamma Ray Bursts

The proceeding set of facts and much more of what was known about GRBs by the 2000s can be found in this review by Tsvi Piran.^[12]

Gamma Ray Burst is the name given to the extremely high gamma photon count extra terrestrial events that were first detected by US Spy satellites in the 1960s. Their most striking feature is their total energy output, which if you calculate based upon the total energy deposited in our detectors and the redshift of the source, gives you an isotropic energy equivalent of 10^{54} ergs. This high energy output means that GRBs outshine the rest of their host galaxies for the duration they are active. Such a high energy output requires a quite violent and explosive event as an explanation and based upon coincident detections of supernovae and neutron star mergers, we can with reasonable degree of certainty conclude that the longer gamma ray bursts tend to originate from supernovae (explained by the so called collapsar model) and shorter ones come from neutron star mergers.^[11]

One of the first questions that tends to be asked of any astronomical observation is what is the spectrum of the emission reaching us and which physical processes explains

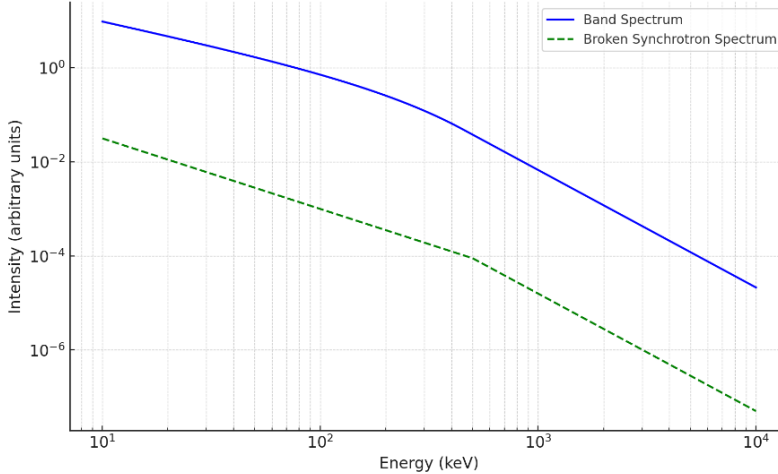


Figure 1.1: Comparison Energy Spectrum of Band and Synchrotron

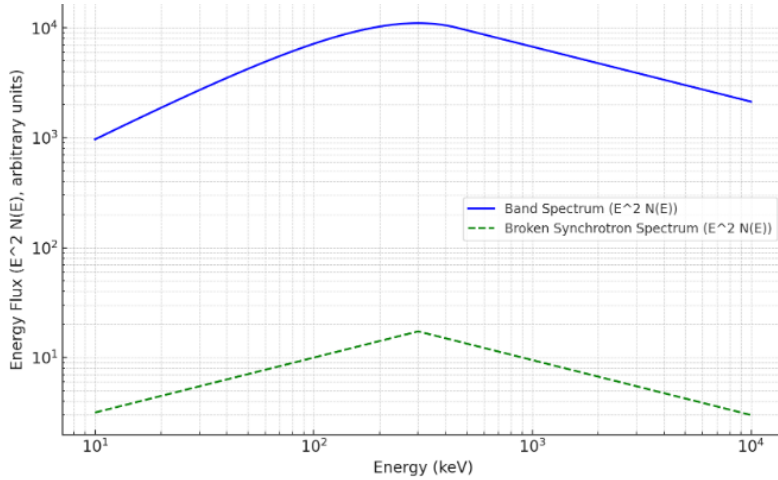


Figure 1.2: Comparison of Energy flux spectrum of Band and Synchrotron

that mode of emission. Unfortunately we do not have a one size fits all equation for the spectrum of a GRB. Many models such as cutoff power law (CPL), Smoothly Broken Power Law (SBPL) and possible blackbody components get used to explain certain aspects of the emission process however none of these can explain the majority of observed spectra on their own. A phenomenological model known as the Band function (named after prominent researcher David Band [2]) has been proposed way back in 1993 that is best described as a two power laws that are joined smoothly at a break energy $(\bar{\alpha} - \bar{\beta})E_0$

$$\frac{dN(E)}{dE} = N_0 \begin{cases} (E)^{\bar{\alpha}} \exp\left(-\frac{E}{E_0}\right) & \text{for } E < (\bar{\alpha} - \bar{\beta})E_0; \\ [(\bar{\alpha} - \bar{\beta})E_0]^{(\bar{\alpha}-\bar{\beta})} (E)^{\bar{\beta}} \exp(\bar{\beta} - \bar{\alpha}), & \text{for } E > (\bar{\alpha} - \bar{\beta})E_0, \end{cases}$$

This spectrum has the same basic shape when compared to the shape of the Synchrotron spectrum except that the sharp breaks are replaced by smooth transition between the low energy and the high energy indices. The following plot of the energy spectrum of both of them is very telling.

The highly energetic matter and likely strong magnetic fields in the vicinity of the jet makes Synchrotron radiation of the primary candidates for the dominant emission process however with many unknown features such as jet geometry, magnetic field structure and

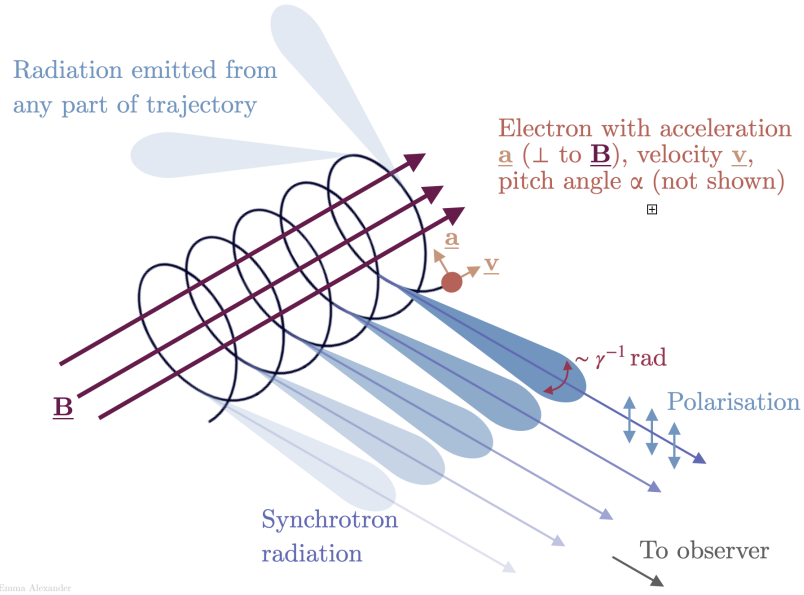


Figure 1.3: Visualisation of polarised Synchrotron radiation by Emma Alexander

outflow composition we end up with not much in the way of constraining the emission mechanism using the resulting spectral measurements.

This is where spectro-polarimetry becomes important as the information contained in the linear polarisation of all bursts has been proposed as a way to discriminate between combinations of the above unknown features^[6] and the use of ensemble properties of the observed polarisation of various bursts has been proposed as pathway to hone in on the true emission mechanism.^[7] To see this in detail we have to look into how polarisation is represented analytically and how it is applied in the context of jet physics.

1.2 Theory of polarisation

When hot and ionised matter is subjected to magnetic fields, radiation is expected to be seen and Synchrotron in nature. Not only that, but every local fluid element will have a definite dependence of the polarisation vector on the local magnetic field at that point. GRB spectro-polarimetry has been mostly studied with Linear Polarisation in mind. To describe all possible states we want to study, we need to define some parameters to describe their features. This is done in two major ways; using the Stokes parameters and the Poincare Sphere. In the following section I follow the discussion of these quantities given in the papers by Kenji Toma ^[15] and Ramandeep Gill. ^[7]

1.2.1 Stokes' Parameters

Stokes' parameters let us define the linear polarisation in terms of the several components of the final intensity of the electromagnetic wave. Most simple to understand is I , the total intensity of the propagating wave defined simply as the sum of the Intensities in the x and y directions or any other set of perpendicular directions.

$$I \equiv \langle E_x^2 \rangle + \langle E_y^2 \rangle = \langle E_a^2 \rangle + \langle E_b^2 \rangle = \langle E_r^2 \rangle + \langle E_l^2 \rangle,$$

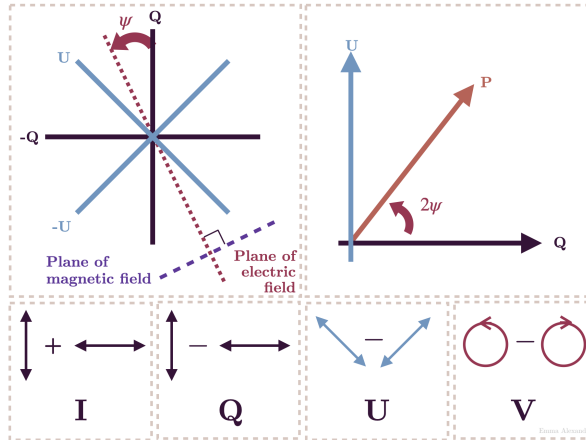


Figure 1.4: Visualisation of Stokes' Parameters by Emma Alexander

Q and U are defined as the difference in intensities of two different sets of perpendicular axes, rotated at $\pi/4$ angle to the other. V is not going to be relevant for our discussion as it deals with circular polarisation, yet I've given it for completeness.

$$Q \equiv \langle E_x^2 \rangle - \langle E_y^2 \rangle, \quad U \equiv \langle E_a^2 \rangle - \langle E_b^2 \rangle, \quad V \equiv \langle E_r^2 \rangle - \langle E_l^2 \rangle.$$

1.3 The Poincare Sphere

For our purposes, these parameters can be mapped to a sphere as well called the Poincare sphere where Q , U and V are on the coordinates axes and I represents the radius of the sphere as a whole. In this representation, a fully polarised beam of light lies on the surface of the sphere as all its constituents have some non-random polarisation, and everything else lies somewhere inside the sphere itself. This gives us a neat way of thinking about the polarisation fraction (PF) of the in terms of the stokes parameters themselves:

$$\Pi = \frac{\sqrt{Q^2 + U^2 + V^2}}{I} \tag{1.1}$$

It is noteworthy that these parameters are useful to make predictions insofar as we can associate some value of these parameters to every fluid element of the jet exactly. After assuming some spectrum of emission (such as synchrotron for every electron) we need to integrate over all the fluid elements of that jet, with the jet geometry in mind to get the complete polarisation picture we should expect to see.

1.3.1 Micro-polarisation to macro-polarisation

The following integration is extremely important to the jet modelling of GRBs as it lays the groundwork for discussing more complicated jet geometries in the future, and gets us closer to a complete understanding of what polarisation signatures mean physically speaking.

$$I_\nu = \frac{1+z}{d_L^2} \int d\phi \int d(\cos \theta) r_0^2 \frac{A_0 f(\nu')}{\gamma^2 (1-\beta \cos \theta)^2} \tag{1.2}$$

Here I_ν represents the total Intensity from a certain ν in the observer's frame emanating from a spherical fluid element moving at relativistic speeds and having a spectral function (ν') where the primed coordinates are in the emitter's frame.

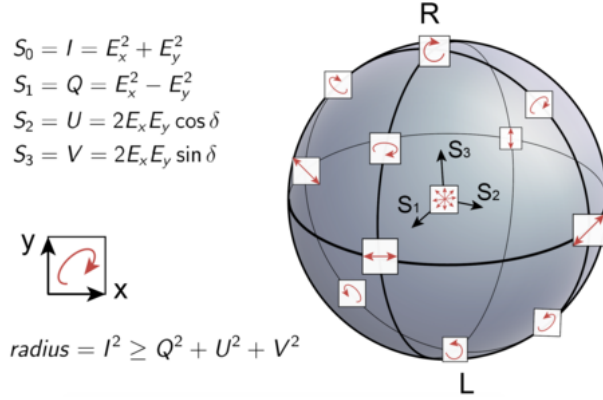


Figure 1.5: The Poincare Sphere

U_ν and V_ν are easily related to I_ν given the relation between them shown in Figure 1.2 and the entire expression can be integrated to get the values of each in a waveband $[\nu_1, \nu_2]$. Ψ is the polarisation angle and will henceforth be referred to as PA.

$$\left\{ \begin{array}{c} Q_\nu \\ U_\nu \end{array} \right\} = I_\nu \left\{ \begin{array}{c} \cos(2\Psi) \\ \sin(2\Psi) \end{array} \right\} \quad \{I, Q, U\} = \int_{\nu_1}^{\nu_2} \{I_\nu, Q_\nu, U_\nu\} d\nu$$

Now we must assume a spectral shape. Many models have been discussed in the literature including synchrotron, compton drag etc. However in this chapter I will discuss synchrotron emission with a toroidal field in the plane of the jet which is a variant of the SO model (synchrotron + ordered magnetic field). Jet is assumed to be symmetric and top hat for now.

$$\tilde{f}(x) = \begin{cases} x^{-\alpha} e^{-x} & \text{for } x \leq \beta - \alpha \\ x^{-\beta} (\beta - \alpha)^{\beta - \alpha} e^{\alpha - \beta} & \text{for } x \geq \beta - \alpha. \end{cases}$$

Synchrotron emission has a maximum polarisation fraction given by the following relation in its spectral indices, under assumptions given in [?] for pitch angle and energy distribution, this comes out to be:

$$\Pi_{max}^{syn} \equiv \begin{cases} (\alpha + 1) / (\alpha + \frac{5}{3}) & \text{for } x \leq \beta - \alpha \\ (\beta + 1) / (\beta + \frac{5}{3}) & \text{for } x > \beta - \alpha. \end{cases}$$

Since for optically thin synchrotron emission $\alpha \geq -0.33$ we can see $\Pi_{max} \geq 0.5$. Finally we can substitute the following parameterisations into the integral 1.2 for easy numerical computation:

$$\sin \theta'_B = \left[\left(\frac{1-y}{1+y} \right)^2 + \frac{4y}{(1+y)^2} \frac{(a - \cos \phi)^2}{1 + a^2 - 2a \cos \phi} \right]^{1/2} \quad \chi = \phi + \arctan \left(\left(\frac{1-y}{1+y} \right) \frac{\sin \phi}{a - \cos \phi} \right)$$

where $a = \theta/\theta_v$. Then the formulation of the net polarization degree in the observed frequency region $[\nu_1, \nu_2]$ according to 1.1 becomes [15]

$$\begin{aligned} \Pi = & \left| \int_{\nu_1}^{\nu_2} d\nu \int_0^{(1+q)^2 y_j} \frac{dy}{1+y^2} \right. \\ & \times \int_{-\Delta\phi(y)}^{\Delta\phi(y)} d\phi \tilde{f}(x) (\sin \theta'_B)^{\alpha+1} \Pi_0^{\text{syn}}(x) \cos(2\chi) | \\ & \times \left. \left[\int_{\nu_1}^{\nu_2} d\nu \int_0^{(1+q)^2 y_j} \frac{dy}{(1+y)^2} \int_{-\Delta\phi(y)}^{\Delta\phi(y)} d\phi \tilde{f}(x) (\sin \theta'_B)^{\alpha+1} \right]^{-1} \right. \end{aligned}$$

where $q = \frac{\theta_v}{\theta_j}$, $x = (1+z)\nu(1+y)/2\gamma\nu'_0$, $\xi_j = y_j = (\gamma\theta_j)^2$. ‘q’ represents the ratio between the viewing angle and top-hat jet opening angle and ξ loosely tells us how fast the bulk of jet is moving. The following is a numerical plot of the above expression for various values of alpha. As can be seen, the higher the low energy spectral index (corresponding to a softer GRB spectrum) the greater is the expected PF, as a ratio of the theoretical maximum PF.

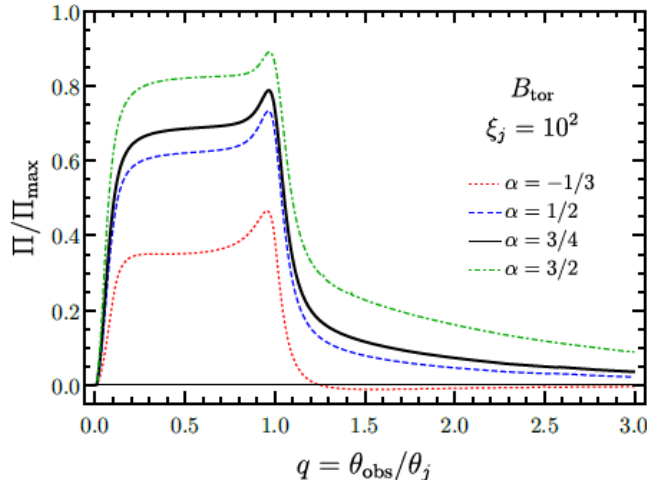


Figure 1.6: Synchrotron Emission with Toroidal field^[6]

Two important effects need to be understood to rationalise the behaviour of a plot like this which are symmetry breaking and relativistic beaming.

1. $q=0$ represents an on-axis observer. When viewing is axisymmetric, PF is expected to be zero since we have assumed a toroidal magnetic field and all the polarised light reaching the viewer from various parts of the jet would cancel out leading to essentially randomly polarised light.
2. As we move towards the edge of the jet at $q=1$, the B field has non-zero gradients and the PF shoots up. At $q=1$, we have maximum symmetry breakage since there is no intensity coming from outside the top-hat jet, and thereafter it dies down.
3. The synchrotron radiation is relativistically beamed and thus near $q \in \{1 - \gamma^{-1}, 1 + \gamma^{-1}\}$ we see rapid changes in behaviour as the light cones reaching the viewer drop off in intensity quickly from many fluid elements at once, and nothing replaces them which happens inside the bulk.

1.4 Importance of Polarization to GRBs

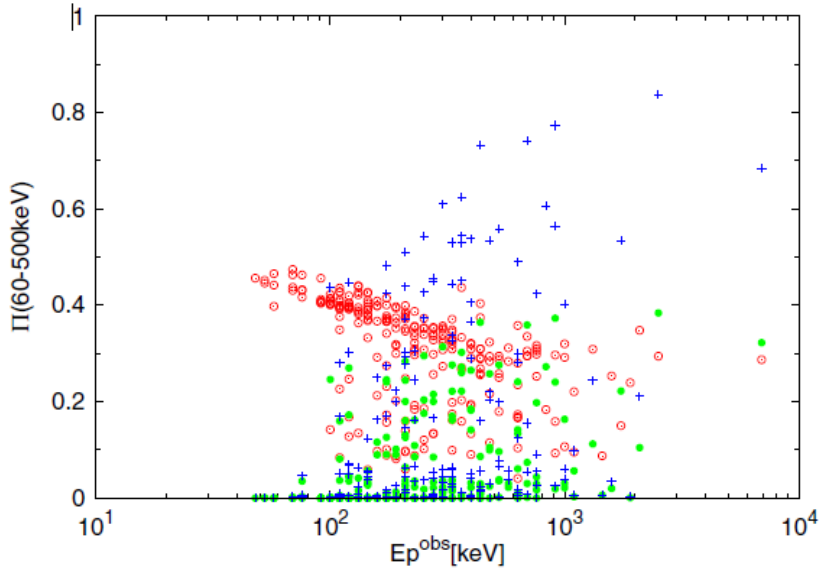


Figure 1.7: Red - SO model, Green - SR model, Blue - Compton Drag model

The most important part of the GRB Polarimetrist's tool kit is knowledge of ensemble predictions. To discriminate between various models we must make testable predictions and in this case of the various models proposed such as Synchrotron Ordered (SO), Synchrotron Random (SR) with $\langle B_R^2 \rangle \gg \langle B_{ord}^2 \rangle$, or the compton-drag model (CD). Repeating similar calculations as in the previous section for top hat jets with all these models and making reasonable assumptions regarding viewing angle, distance of source, spectral indices and mass model of a particular satellite called POET, Toma et al [15] reached the following distribution of the detectable bursts out of 10,000 simulations for each model in the energy range 60-500 keV. This allows us to make the following conclusions, which are not universal but illustrate how discrimination between models would work in these scenarios.

1. The Compton drag model seems to register high PF values. Going up all the way to 0.8 even, which is in stark contrast to the synchrotron models. This is most likely due to the Compton drag model not having an upper bound on max polarisation, admitting upto PF=1 for each fluid element. A significant number of high PF bursts would thus bring the CD model back into relevance for atleast those GRBs.
2. SO model seems to be clustered around a PF of 0.3, which means if we are able to secure polarisation measurements for many GRBs around this range it could further solidify the incumbent toroidal field as the most viable explanation for GRB emission.
3. A large clustering of near-zero PF would be evidence against the SO model, however would lead to degeneracy between SR and CD. This is where spectroscopy would come handy to differentiate between SR and CD.

Chapter 2

Detecting x-rays and γ -rays

High energy photons have three dominant kinds of interactions when interacting with matter; they are the Photoelectric Effect, Compton Effect and Pair-Production. There is no deterministic way of deciding which photon will undergo what interaction and when, there are no hidden variables after all and the best description we have is that of probability density function for all of these photons anyway. All of this means that we can only define relative probabilities for these interactions to occur and this is done in terms of their individual scattering cross section.

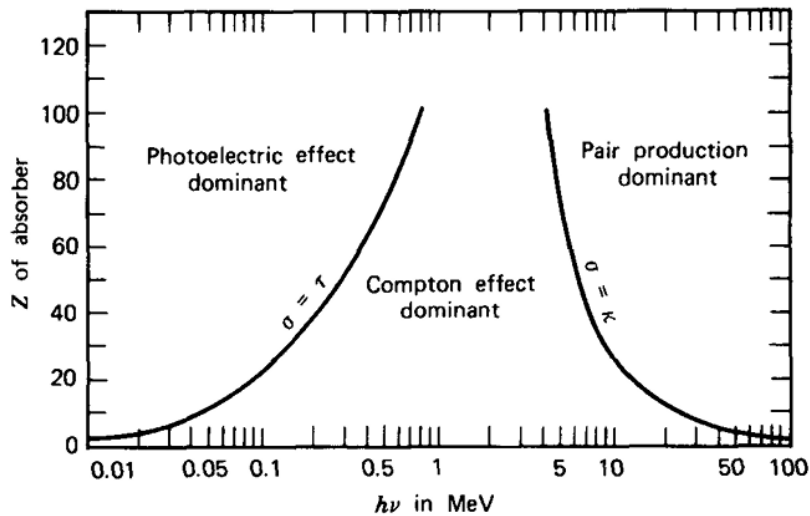


Figure 2.1: Figure showing dominant process for various Z and $h\nu$ ^[8]

Looking at the figure above, we can see that as the atomic number increases the relative probabilities change, and the solid line represents the curve for where the dominant interaction (defined by highest magnitude of cross section) switches over to another. As an example, the Cadmium Zinc Telluride (CdZnTe) inside the AstroSat CZTI has an effective atomic number of about 53, and the typical x-ray energies encountered is above 100 keV for doing polarimetry which means comptonisation is the main interaction we can expect to occur, if the photon interacts at all.

The effective cross section the electron sees is the sum of the cross sections of all of these processes. This gives rise to the attenuation coefficient which will appear later as well when I discuss simulations however even for now it is helpful remembering the attenuation coefficient depends on the energy of the photon and atomic number of the absorber in quite non trivial ways. Meaning the success or failure of a mission could very well be decided on whether a correct choice of material was made for the actual detector or not. The overall density of the material has to be taken into account as well making

the parameter called the mass attenuation coefficient important in deciding if the photon is likely to interact or not. The mass attenuation coefficient is given by :

$$\frac{\mu}{\rho} = \frac{\sigma_{total}}{uA} \quad \text{and} \quad \sigma_{total} = \Sigma \sigma_{individual}$$

2.1 The Compton Effect

The basic energetics of the Compton effect are well understood. Given the initial energy of the incoming photon and the azimuthal scattering angle of the photon itself, we can apply momentum and energy conservation in the relativistic regime :

$$\begin{aligned} hf + m_e c^2 &= hf' + \sqrt{(p_{e'} c)^2 + (m_e c^2)^2} \\ p_{e'}^2 &= \mathbf{p}_{e'} \cdot \mathbf{p}_{e'} = (\mathbf{p}_\gamma - \mathbf{p}_{\gamma'}) \cdot (\mathbf{p}_\gamma - \mathbf{p}_{\gamma'}) \\ &= p_\gamma^2 + p_{\gamma'}^2 - 2p_\gamma p_{\gamma'} \cos \theta \end{aligned}$$

After replacing the photon momentum terms with hf/c , we get a second expression for the magnitude of the momentum of the scattered electron which, after evaluating the square and canceling and rearranging terms, further yields

$$\lambda' - \lambda = \frac{h}{m_e c} (1 - \cos \theta)$$

This however does not tell what is crucial to us however; which is the actual probability of getting a particular scattering direction, given the incoming energy of the photon. To actually calculate that, we would have to take into account the interaction of the electromagnetic wave with the internal states of the atom in question, which is unfortunately outside the scope of this report. Regardless, in the further sections I will describe the implications of the theoretical result and how it's used in actual instruments.

2.2 The Klein-Nishina Cross Section

Oskar Klein and Yoshio Nishina derived the following formula in 1929 [18] for the cross section using the Dirac equation proposed in the same year. It served as one of the first testable predictions for Dirac's theory and gave it mainstream appeal when it was verified by actual X-ray interaction experiments. Key things to note about this formula are that θ is the polar angle defined with respect to the direction of the incoming photon(generally assumed to be along z) and ϕ is the azimuthal angle, defined with respect to the polarisation direction of the incoming photon.

$$\frac{d\sigma}{d\Omega} = \frac{r_0^2}{2} \left(\frac{E}{E_0} \right)^2 \left(\frac{E_0}{E} + \frac{E}{E_0} - 2 \sin^2 \theta \cos^2 \phi \right)$$

In the case of classical scattering (such as rutherford scattering for inverse square potentials) the differential cross section is interpreted in a deterministic sense where we track the actual trajectory of the particle, incident at some incremental area corresponding to an infinitessimal change in the impact parameter, which gets mapped to an incremental spherical area element. If you then assume all the incident particles to be uniformly distributed at all impact parameter values, you can interpret the normalised differential

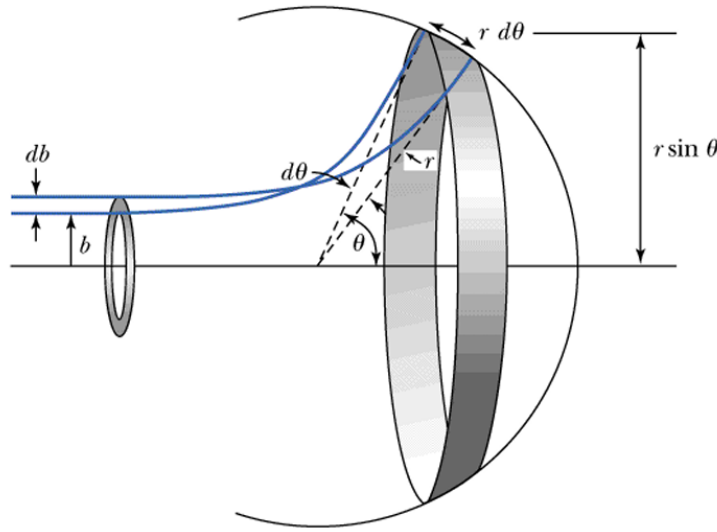


Figure 2.2: Schematic description of classical scattering

cross-section as the probability density which you can expect the spherical elements to have.

However in quantum mechanical scattering, the differential cross section can only be interpreted in terms of probability densities from the start as only wave functions are defined. The potential of the scatterer essentially “morphs” or “operates” on the incoming wavefunction and creates new scattering eigenstates of the form:

$$\Psi(r) = e^{ikz} + f(\theta, \phi) \frac{e^{ikr}}{r}$$

Where f is dependent on the exact form factor of the potential or interaction being talked out. Hence the scattering cross section $\frac{d\sigma}{d\Omega}$ is proportional to the probability of obtaining a measurement at that location given the incident wave function was a plane wave e^{ikz} along the z direction:

$$P(\theta, \phi) = \frac{1}{\sigma_{KN}} \frac{d\sigma}{d\Omega}$$

σ_{KN} is the total scattering cross section that must be obtained by performing the integral of $\frac{d\sigma}{d\Omega}$ over $\sin\theta d\theta d\phi$ giving us :

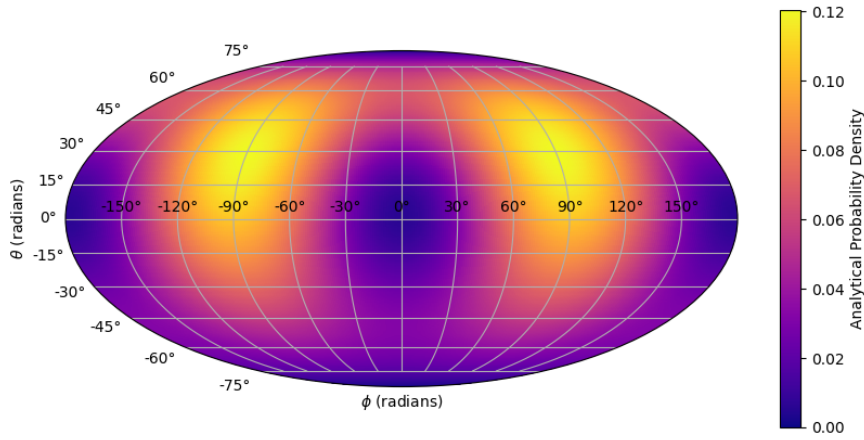
$$\sigma = 2\pi r_e^2 \left[\frac{1+\epsilon}{\epsilon^3} \left(\frac{2\epsilon(1+\epsilon)}{1+2\epsilon} - \ln(1+2\epsilon) \right) + \frac{\ln(1+2\epsilon)}{2\epsilon} - \frac{1+3\epsilon}{(1+2\epsilon)^2} \right]$$

Where ϵ is the ratio of incoming energy and $m_e c^2$ and r_e is the classical electron radius. As a side note, averaging over all values of azimuthal angle (all being equally likely) lets you retrieve the unpolarised cross section :

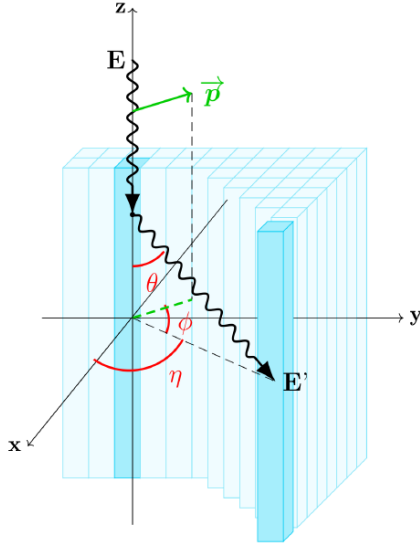
$$\frac{d\sigma}{d\Omega} = \frac{r_0^2}{2} \left(\frac{E}{E_0} \right)^2 \left(\frac{E_0}{E} + \frac{E}{E_0} - \sin^2 \theta \right) ; \quad \langle \cos^2 \phi \rangle = 0.5$$

2.3 The Modulation Curve

Looking at the KN cross section we find that the probability density function clearly is minimum at $\phi = 0$ and maximum at $\phi = \pm\pi/2$.


 Figure 2.3: Analytical Heat Map for $E = 200\text{keV}$

Which simply means that the scattering of the incoming photon happens preferentially in the direction perpendicular to the initial polarisation direction. This is an important result as now we have the means to make testable predictions regarding the polarisation of the incoming rays based off of the scattered photon direction.


 Figure 2.4: Visualisation of Compton Scattering within the POLAR detector^[9]

The way this is usually achieved in the instruments is by the construction of the modulation curve which is the distribution of the compton scattered electrons in each azimuthal angle bin of a pixellated detector. However I shall discuss this in the next chapter as before diving into detection of polarisation we must discuss the basic detection principles of these detectors.

2.4 Relevant Detection Principles

The key to a polarization measurement is the measurement of two interaction positions within the detector. This is because the most direct way to calculate the Compton scattering angle is via two interactions of the photon within the polarimeter: an initial Compton scattering interaction followed by either a second Compton scattering or a photo-absorption. The position resolution for the two interaction locations determines the precision in the scattering angle measurement, which translates to the precision of the polarization measurement. Polarimeters therefore require either a position sensitive detector material, such as a silicon strip or pixel detector, or a segmented detector, for example a scintillator array. The former is complex and typically has a low cross section for Compton scattering in the 10–100 keV energy range where the majority of the flux is. Scintillator arrays have a worse position resolution but allow for a large, relatively low cost, low power, scaleable detector efficient at lower energies.

Following is the quoted description of the POLAR^[9] instrument aboard China's Tiangong 2 Spacecraft which was built explicitly for polarimetry purposes :

The POLAR detector makes use of a segmented scintillator array. The full plastic array comprised 1600 scintillator bars with a dimension of $5:8 \times 5:8 \times 176 mm^3$. The use of plastic scintillators over high Z materials, such as for example silicon detectors, increases the probability for photons to Compton scatter in the detector especially at energies below 100keV. The downside of a purely plastic based detector compared to a detector consisting of a combination of plastic and a high Z scintillator, such as that used in GAP, is the lower stopping power after the initial interaction. After Compton scattering the photon can undergo several Compton scattering interactions or even leave the polarimeter, thereby reducing the efficiency.

and similarly, here is the quoted description of the CZTI imager aboard AstroSat^[16], which I will discuss extensively in this work.

The Cadmium-ZincTelluride Imager (CZTI) onboard Astrosat, which is primarily designed for hard X-ray imaging and spectroscopy, is one instrument expected to be sensitive to the polarization of the incident X-rays thanks to its large pixilated detector plane. The CZTI is a coded aperture mask telescope with a total active area of 1024 cm². The detector plane consists of 64 detector modules arranged in four identical quadrants, each having 16 modules arranged in a square geometry. Each module is an independent cadmium-zinc-telluride (CZT) detector with a 16×16 array of pixels, each $2.5 \text{ mm} \times 2.5 \text{ mm}$. The 5 mm detector thickness provides detection efficiency at energies higher than the primary spectroscopic energy range of 10 keV to 100 keV, where a significant fraction of photon interaction occurs by means of Compton scattering. In these events, the Compton-scattered photon could be detected in an adjacent pixel. Since the direction of the scattered photon depends on the polarization direction of the incident photon, such pixelated detectors can, in general, and for Astrosat-CZTI, in particular, be used as a Compton X-ray polarimeter.

Chapter 3

GRB Compton Polarimetry

Owing to the great interest in the astronomical community regarding the study of GRBs, a large number of space telescopes and detectors are currently up and running for that very purpose. GRB names reveal a lot about the nature of their detection, in that a typical name is a concatenation of 'GRB' with the date in YYMMDD format, followed by alphabets A,B,C indicating the first second third and so forth GRB of that day. Upon browsing the table of observed GRBs on a website like [this](#) we notice two things : some days go by where no GRBs are detected at all and there are days with several GRBs. This simply points to the unpredictable and essentially random nature of detecting GRBs. Another noticeable feature is the fact that GRBs are isotropically distributed in the sky (which was one of the ways they were proven to be extra-galactic). Implying that until and unless we have a telescope or set of telescopes capable of looking at every single part of the sky, at all points in time, we will always be missing some GRB or the other.

3.1 State of GRB Polarimetry

Currently the only secure polarisation measurements that have been made on GRBs have all been based on the Compton Effect. To be even more specific we have based them on Compton scattering within the detector with only one exception where the BATSE instrument tried to use compton scattering off the Earth's atmosphere^[7].

The events we have ended up calling GRBs typically have had count rates above the observed background of gamma rays in the range of few hundred per second, depending on the energy range of that detector. The brightest GRB of all time (lovingly called the BOAT) GRB 221009A had a peak count rate of above 23,000 counts per second and it was also 70 times brighter than the previous brightest GRB 130427A^[17]. These kinds of count rates are enough to get really secure spectral fits and for a long time now, time resolved spectroscopy has been achievable on most GRBs. Yet, of the thousands of GRBs detected and spectrally analysed, a polarisation analysis has been performed on a minuscule fraction. In CZTI's 5 year polarisation catalog^[5], the polarisation analysis of 20 GRBs was done and even of them only 5 of those had secure Bayes factors of more than 3, in favour of the hypothesis that a non-zero polarisation fraction (PF) was present. This pales in comparison to the about 500 GRBs that had been detected by CZTI at the time. By 2021, the gamma ray polarisation analysis of only 31 GRBs have been published despite several missions being operational for many years.

Time-resolved measurements are even more rare as breaking the burst into time bins often doesn't lead to enough Compton counts in those time bins to get secure polarisation measurements. Therefore most analyses, such as those conducted by POLAR and CZTI, utilise the entire burst which could be problematic for two reasons^[7]:

1. Assuming the original burst did have an evolving PA and PF, we would wash out much of that variation by looking at the entire burst, leading to lower PFs in general and some other PA than the individual.
2. Many GRBs do have multiple separated emission episodes in their light-curve structure and we know the spectral variation with time. Therefore from a mechanistic point of view we would expect different emission episodes to not have the same PF and PA since they possibly have different mechanisms responsible for those counts, occurring at spatially and temporally separated regions of the source.

For both these reasons it is imperative we obtain more secure polarisation measurements of more GRBs. The POLAR Collaboration has shown a only hint of time varying PA for two of its analysed bursts [10] meanwhile the AstroSat team managed to break the GRB 160821A into three distinct time intervals and get secure results (3σ) for each of them[13]. Similar analysis by them showed GRB 160325A^[14] as significantly polarised when time integrated however the first emission episode was found to have no or low polarisation and the second one a high PF albeit only at 1.5σ confidence level. Single peak GRBs are of some importance as they are thought to be the 'clean' and uncontaminated emission episodes and there is no evidence of PA varying within such a Fast-Rise Exponential Decay (FRED) peak^[7].

Now in the rest of this chapter I will explain in-situ compton effect based polarimetry with heavy reference to the working of AstroSat CZTI and even compare it to POLAR.

3.2 Compton Double Counting in Practice

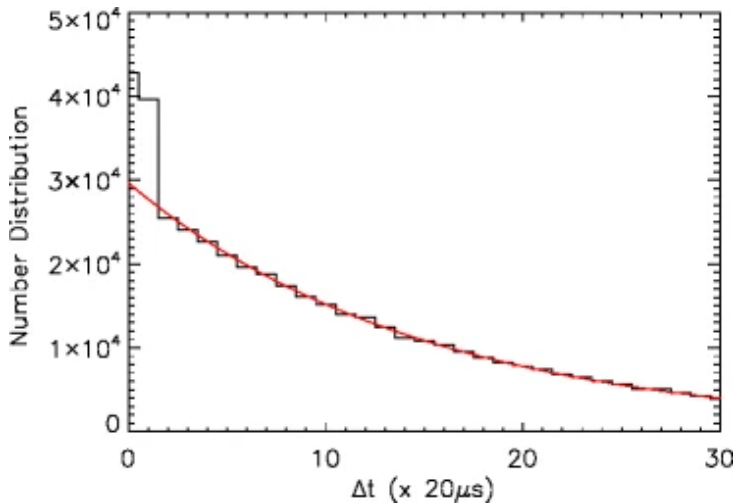


Figure 3.1: Histogram of time intervals between events for a CZT detector [4]

Given the previous chapter's explanation of the motivation behind the modulation curve, it must be clear that building the histogram of scattering angles based upon the pixellated detector set up is the name of the game. The readout logic of CZTI is such that all events occurring in the same $20\mu s$ time bin get tagged with the same time stamp. Given the fact that it would take the comptonised photons about a few nanoseconds to escape the detector if they don't interact with the detector itself. Therefore it is reasonable to conclude that if the comptonised photon interacts again in the detector, it would be having

the same time stamp and would be visible as the excess above the poisson distribution that is generally followed, in the first few bins of the histogram of time between successive events. That is exactly what was found by Chattopadhyay et. al. in [4] in figure 3.1 in their experiment on CZT detectors with ^{57}Co samples. In reality, not just the first but the second time bin sees a significant bump, this is due to the specific readout logic of the CZTI. There are a lot of other components of this non-poissonic excess and I shall therefore go on to describe the exact methodology developed to retain only the genuine compton events.

3.2.1 Role of Geant4 simulations for CZTI



Figure 3.2: Actual Photo of the AstroSat CZTI

Creating the response file for any detector is crucial in analysing its readouts. The process of creating CZTI's response file involves entering a detailed mass-model for the entire AstroSat into Geant4, deciding upon a location in the sky which represents where the GRB is coming from in relation to the orientation of the detector, selecting a spectrum to draw photons from, their PA (defined with respect to the incoming direction) and PF, number of photons to simulate, and finally which interactions to track within the detector itself. In the CZTI pipeline, we get the output file called 'EventFile(seed-number).txt' which contains 60 columns! some of which are: photon ID, number of photoelectric interactions, number of compton interactions, location and energy data for 7 interactions, location and energy of up to 3 brehmsstrahlung interactions and CsI-Veto detections.

Ultimately from this data we have to find the genuine Compton counts to properly build the response matrix. The criteria for that are next.

3.2.2 Kinematic and Energetic Criteria

I have mentioned already the excess counts within the $40 \mu\text{s}$ time window, however a large number of them are purely due to chance as can be seen by extrapolating the poisson distribution backwards. Randomly removing some amount isn't going to work as

we require the scattering information of the valid compton counts and blindly removing some would defeat that purpose. Hence the first criterion applied is kinematic in nature which is that :

- Only interactions in 8 nearest-neighbour pixels are valid compton events

Key reasoning being that it is unlikely for the scattered photon to travel very far inside the detector given the mean free path of these photons meanwhile a random coincident event could appear anywhere in any pixel. After this, another criterion based on energetics has to be applied to remove the remaining chance coincidence events remaining which is :

- The energy of the comptonised photon is always greater than the scattered electron for incoming energies less than 280 keV, and for scattering with polar angles around $\pi/2$, ratio of energy deposited in adjacent pixels is between 1 and 6.

This can be easily derived from the fact that the fraction energy carried away by the photon and electron are respectively:

$$\frac{E'}{E} = \frac{1}{1 + \frac{E}{511}(1 - \cos\theta)}; \frac{E_e}{E} = \frac{\frac{E}{511}(1 - \cos\theta)}{1 + \frac{E}{511}(1 - \cos\theta)}$$

and at electron energies less than about 280 keV, even for $\theta = \pi$, we have $\frac{E'}{E_e} > 1$ and for $\theta = \pi/2$ we have $\frac{E'}{E} \geq 2$. The electron will end up getting absorbed within the same pixel due to significantly lower mean free path thus the assumption of ratio of energy deposited is justified. Both these criteria do a good job together do a good job in removing the inherent spectrum of a radioactive source, as was verified by Chattopadhyay et. al. in [4] in an experiment with Cobalt.

After this we must divide the modules of the detector into pixels and actually assign pixel numbers to each of the interactions. Then we add up the energies deposited in each of the pixels. In doing so we must be careful as the photoelectric effect still lurks inside our results and contaminates the azimuthal angle distribution by diluting out the polarisation signature. Additionally brehmssstrahlung photons from the ejected electron once again could trigger our double pixel events. Hence we must be careful in deciding which the ‘first’ pixel is we do this by considering:

- Of the double pixel events, the pixel with lower energy is the ‘first’ pixel

Once this is done, we can go on to building the modulation curve.

3.3 Building the Modulation Curve

The entire goal of building these geant4 simulations ultimately is to build a library of these modulation curves for various energy ranges and polarisation angles, given an incidence direction of the GRB, to allow comparison with actual in-sky data from any GRB we wish to analyse in the future. In the base analysis pipeline all that is left to do is to actually make the histogram of the counts in each angular bin. A hurdle we have to cross is CZTI’s square pixels make for unequal distances to each of the nearest neighbours, meaning there is an inherent modulation in the azimuthal histogram, with the corner pixels being disfavoured, thus it is important to actually notice the need to normalise these histograms with completely unpolarised beams to obtain the true modulation present only because of the compton scattering.

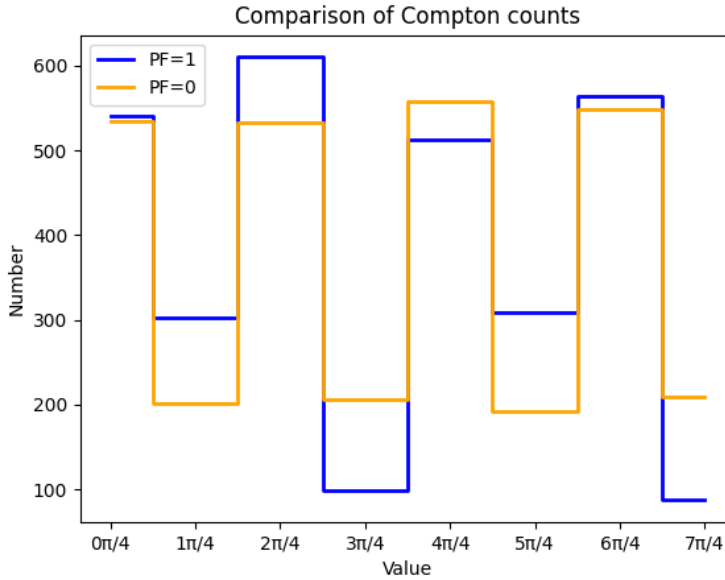


Figure 3.3: Overlaid Polarised and Unpolarised runs

This is done according to the following method^[16]: if $N_{i,pol}$ is the number of counts in the i th bin for 100% polarised beams and $M_{i,unpol}$ is the counts in that bin for a 100% unpolarised beam, we have :

$$N_{i,corrected} = \frac{N_{i,pol}}{M_{i,unpol}} M_{unpol,average}$$

Which gives us the final corrected histogram in the simulations. After all of these steps for the simulation we are ready to repeat these steps except this time use actual instrument read-outs and to measure linear polarisation of the incoming GRBs.

The raw instrument readout also has this geometric effect built-in and has to be normalised with the unpolarised beam the same way. However since the original PA is unknown and PF not necessarily 100 %, we have to perform an inference of some kind. One approach would be to perform a Markov-Chain Monte-Carlo simulation to find the best combination of PA and PF that suits the modulation curve and spectrum of the GRB in question. This is very easily performed in the 'Multi-Mission-Maximum Likelihood Framework' which is a set of python packages really crucial to the analysis of GRBs but for our purposes gives readymade scripts to analyse the event files from instruments such as POLAR and with recent development work I had the pleasure to partake in, CZTI as well. It ends up giving us a fitted set of parameters for the cosine modulation that tells us the PA and PF via the following relations:

$$N(\phi) = A\cos(2(\phi - \phi_0)) + B$$

$$PA = \phi_0 \quad \mu = \frac{A}{B}$$

We would then calculate the value of μ for a completely polarised beam with that same spectrum (μ_{100})and then divide the two to get:

$$PF = \frac{\mu}{\mu_{100}}$$

A drawback of this method is that it assumes the cosine nature of the modulation curve which wouldn't be strictly true for cases with significantly oblique incidences[1]. Another method to find the PA and PF would be to compare the histogram with the library of simulations and find the closest fitting template and assign that value, however this would be computationally quite expensive. Yet off-axis experiments with CZTI detectors have ended up showing that both the methods work equally well even for counts 10 times the compton counts seen in current GRBs. Hence the MCMC approach ultimately wins out [5].

Of course, to maintain statistical significance of the result we usually demand that the Spectral+LinearPolarisation model be fit with a high Bayes Factor of ≥ 3 , and for those without a secure polarisation measurement we at-least try to get some upper or lower bounds on the PA and PF at that high significance level. Ultimately we are limited by the compton counts we receive as part of the GRB detection in getting statistically significant results and the compton efficiency of the detectors.

The earliest polarisation measurements were carried out in an ad-hoc manner by instruments only designed and calibrated to be spectrometers. This leads to somewhat ambiguous results as problems such as a lack of sensitivity owing to unoptimised readout logic for double event selection, ambiguous detector responses due to lack of on-ground calibration and dead material that interferes and fakes polarisation signals.

Now we have many missions specifically designed to be polarimeters and optimised for the same, leading to a large uptick in the analysed GRBs in recent years, coinciding with development on the theoretical models used to talk about GRB Polarisation as well.

3.4 Comparison of AstroSat-CZTI and POLAR

To gain a grasp on what are the ways instruments could differ in their polarimetry I wish to present a simple list of differences between AstroSat-CZTI and POLAR :

1. CZTI is a pixellated CdZnTe hard X-ray imager with a coded aperture mask whereas POLAR contains segmented plastic scintillator detectors, 1600 of them.
2. POLAR fundamentally uses more angular bins and has more complicated systematics and geometrical corrections owing to the fact it doesn't enforce the neighbouring pixel criteria. Since in a plastic scintillator the comptonised photon could reasonably travel further within the detector.
3. CZTI was built for X-ray observations in general and can do spectroscopy in the range 20-200 keV and polarimetry in the range 100-600 keV. POLAR was built for the sole purpose of looking at GRBs in the 50-500 keV range.

So far of all the GRBs analysed by any of these instruments, never has a single common analysis been published. Which means to date we do not have a double confirmation of any of the PA and PF values found by instruments. The necessity of having a joint polarisation measurement cannot be stressed enough as the results can definitely give very secure polarisation measurements if the two instruments are measuring similar things but discrepancies could also inspire new inquiries into the dependency of the prompt emission with energy and the sensitivity of these instruments.

Chapter 4

Monte-Carlo Model and Results of Simulations

Monte-Carlo methods provide us a very accessible way to model otherwise complicated systems and their interactions. For the computational cost of generating a few random numbers according to experimentally found distributions, and applying much simpler physics than a full description would entail, we can model complicated phenomena like the interaction of a detector with radiation and gain predictions for new theories or validations of pre-existing theories. This is precisely what I aimed to do in my set of simulations.

4.1 Assumptions and Scope of the Model

I simulated a 3x3 grid of pixels with the same dimensions as that of CZTI detectors and the scattering of high energy (200 keV) photons via the Compton effect within them. The choice of photon energy was motivated by the fact it is in this energy range does the KN cross section have sufficiently probability of scattering within the same layer of detectors ($\theta \approx \pi/2$) whilst being high enough energy so as to travel significant distances within the detector.

Fundamentally speaking, any incident high energy beam follows an exponentially decaying intensity pattern when it enters into a detector, which means, at the scale of millimetres it is essentially equally probable for any one particular photon to interact with a given layer as any other because all the possible scattering interactions for that photon can be averaged out and replaced with a constant attenuation coefficient.

$$\frac{dI}{dz} = -\mu I \quad I = I_0 e^{-\mu z}$$

For my set of simulations, I pull the distance travelled from an exponential distribution while deciding when a photon actually ends up interacting somewhere in the medium from its point of generation. Furthermore I shall be considering my "detector" to be a 3x3 pixellated array, since practically that is all that should be required to actually recreate the logic used in CZTI's data processing. With all this said here is the algorithm I followed while creating my Monte-Carlo Modulation Curve simulations.

1. Generate a photon of certain energy, incidence direction, PA according to the of the run and start it off at some location uniformly chosen on the bottom face of the central pixel.
2. Take the bottom face to be the x-y plane and pick a random distance from an exponential distribution, considering some attenuation coefficient. If this distance is outside the detector, ignore this photon and go back to step 1.

3. Pick a new direction by sampling from the Klein-Nishina cross section for the incident energy. Rotate the initial propagation vector by that θ and ϕ .
4. Pull from an exponential distribution and see if the new location is within the 8 other pixels. If not, discard and go back to step 1. Assign to a global list one of the 8 values of scattering angle to this valid event.
5. Repeat from step 1 for all remaining photons.

It is most convenient to use rejection sampling whenever an action has to be taken according to a probability distribution such as in step 1 while deciding the PA of the photon. If the simulation run I am doing is completely unpolarised I will pick ϕ_0 uniformly from 0 to 2π . Else if the PF parameter is non-zero, say some 0.25, I will designate ϕ_0 to be a fixed angle (chosen by the user) quarter of the time and any other angle for three quarters of the time.

Rejection sampling is also useful in step 3 when choosing the scattering angle as it gives a straightforward way of obtaining that spherical probability density without having to analytically implement the CDF of the function.

Verifying this rejection sampling is happening properly is indeed a priority otherwise there is no hope of obtaining a valid modulation curve afterward. Thus I present this representative 2D histogram of one of my sampling runs simulated with 200 keV photons. A very clear bias towards $\pm\pi/2$ is observable in both heat maps which bodes well for the

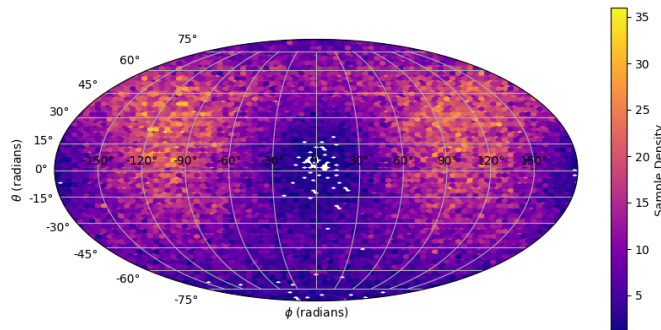


Figure 4.1: Scattering obtained using rejection sampling of $P(\theta, \phi)$

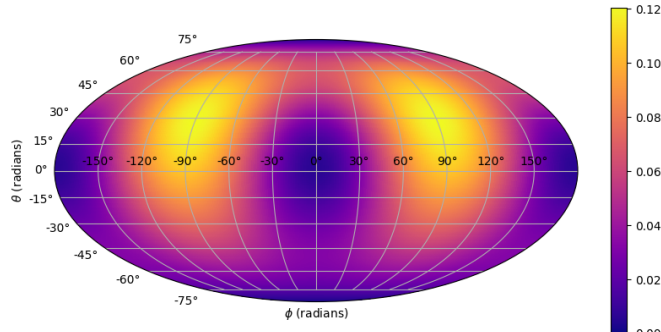


Figure 4.2: Earlier 200 keV map for reference

simulation of the detector itself, since this bias should be directly visible in the modulation curve.

4.2 Histograms of Mono-energetic simulations

Here on I present the results of my mono-energetic monte-carlo simulations that demonstrate the working principle of an instrument like AstroSat-CZTI. The case where the strongest modulation factor should be visible is that of perpendicular incidence as it is in this configuration where the scattered photons would be poised to undergo secondary interactions in one of the 8 nearby pixels.

Firstly the simulation must be done for a randomly polarised or unpolarised beam, i.e. $\text{PF}=0$. Here each photon has a unique polarisation in the x-y plane, and is incident along the $+z$ axis at the bottom of the middle pixel of the detector at a randomly chosen position. Following is the unpolarised histogram for a such a monoenergetic beam of 300 keV energy.

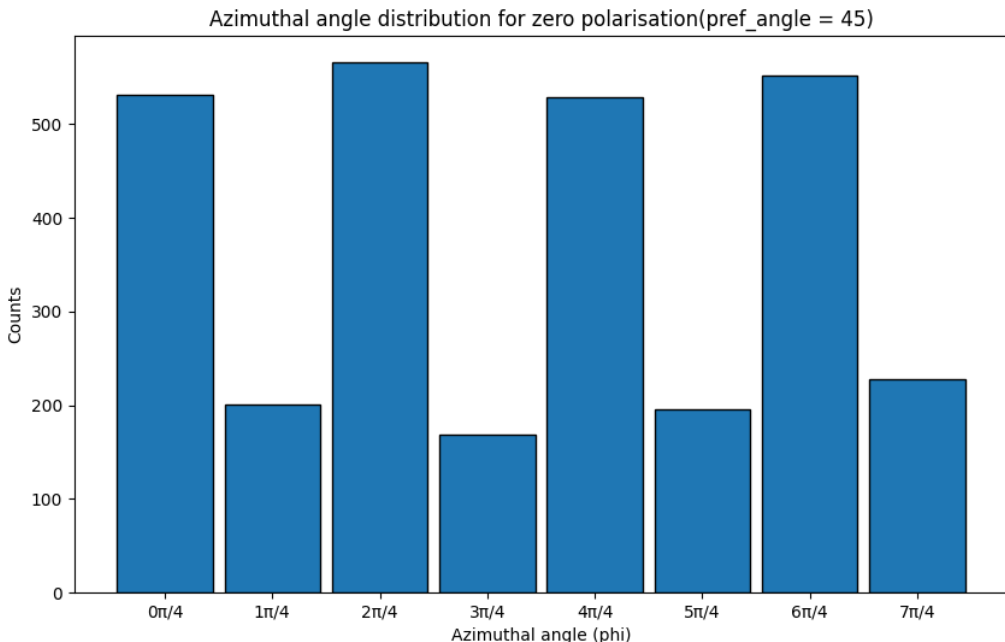


Figure 4.3: Unpolarised raw histograms

As is clearly visible in the figure, there is an inherent bias towards having more scattering in the bins corresponding to the edge pixels of the detector since the corner pixels are simply further away and less likely to be the site of secondary interaction. Now to see the behaviour of polarised light, I simulated two fully polarised beams, with polarisation vector along the x axis and along the $y=x$ line.

In these, interestingly we see a natural preference for two angular bins, in the leftward figure these are the third and seventh bins (corresponding to scattering along $\pm y$ axis) and in the other figure the first and fifth bins (corresponding to scattering along $\pm x$ axis). Still there is inherent geometric effects due to the unequal distances thus we have to apply the histogram correction with the unpolarised run from before and doing so we obtain a clear modulated signal in Figure 4.5.

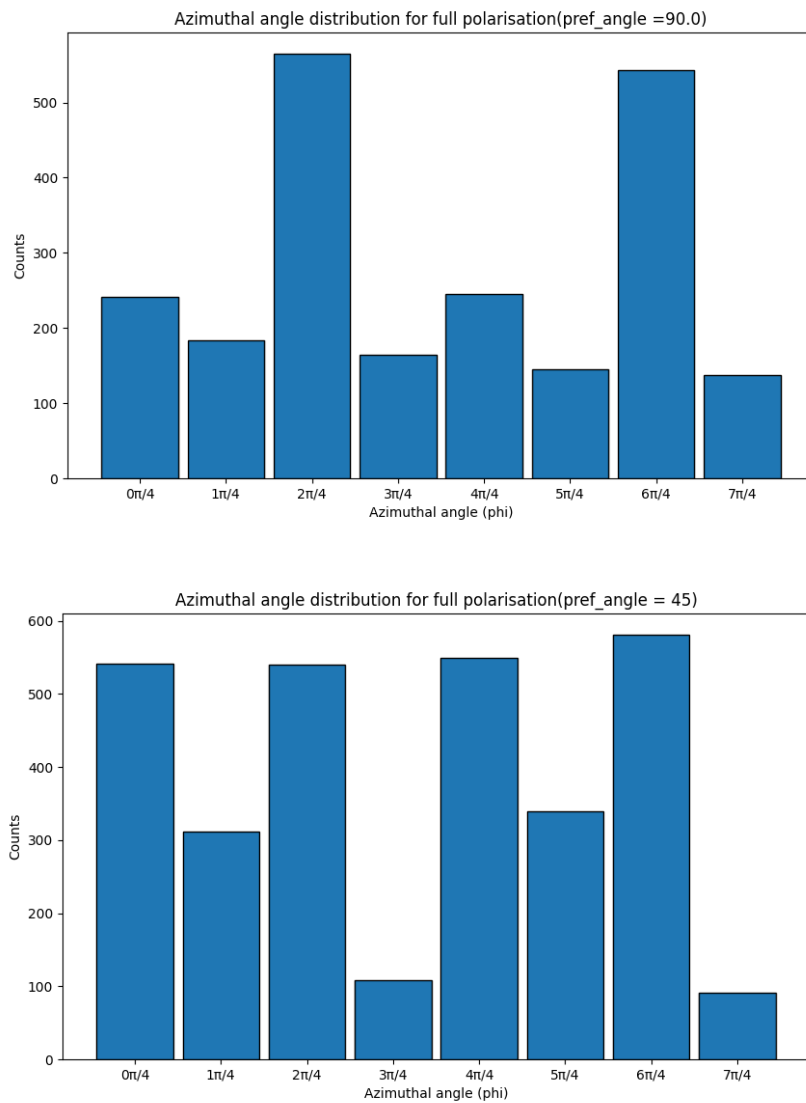
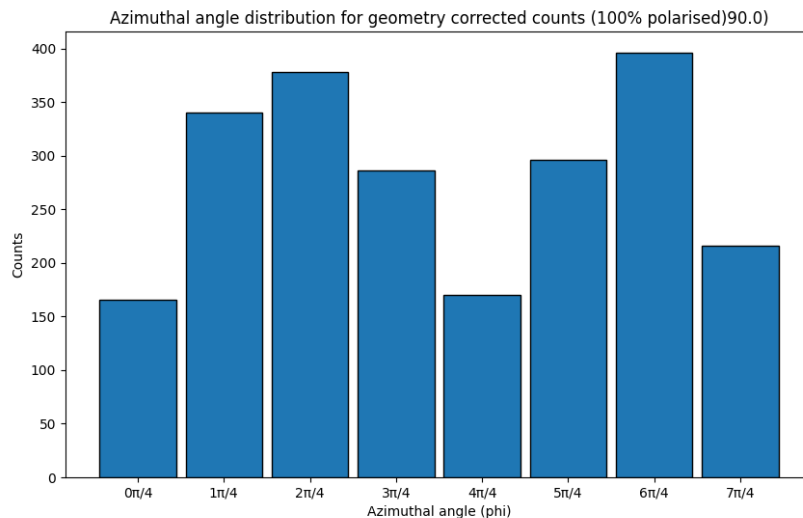


Figure 4.4: Initial, raw histograms, for Y=X and X axis polarisation



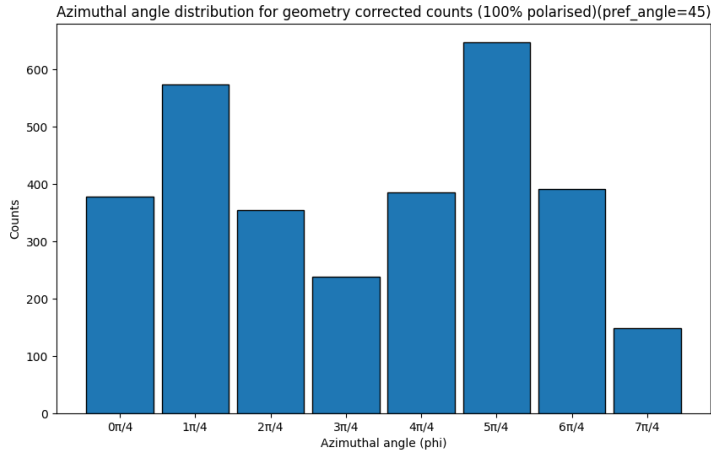


Figure 4.5: Geometry corrected counts for X axis and Y=X polarisation

Two sinusoidal looking curves with different peaks can now sit on both, to confirm that the cosine form of the modulation curve is indeed a good fit, I overplot the best fit curve from the routine in red, and in lower opacity, a 100 curves sampled from the multivariate gaussian of A, B and ϕ_0 with covariances as returned by curvefit in figure 4.6.

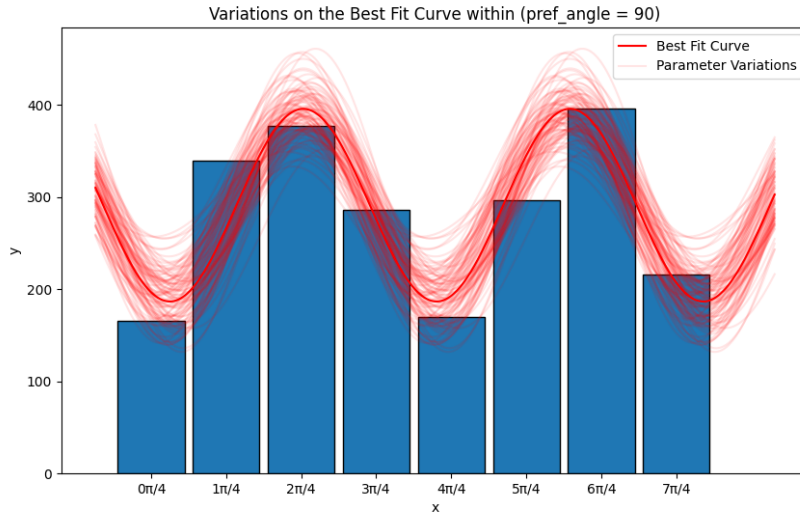


Figure 4.6: Results of curve fitting on X axis polarised

As is visible, the statistics in this case allow for relatively precise construction of the modulation curve. Yet in the following sections, for a lack of valid compton counts, it will be much more difficult to arrive at a well fitting modulation curve like this on the geometry corrected histograms, which is ultimately what makes GRB polarimetry such a photon-hungry pursuit.

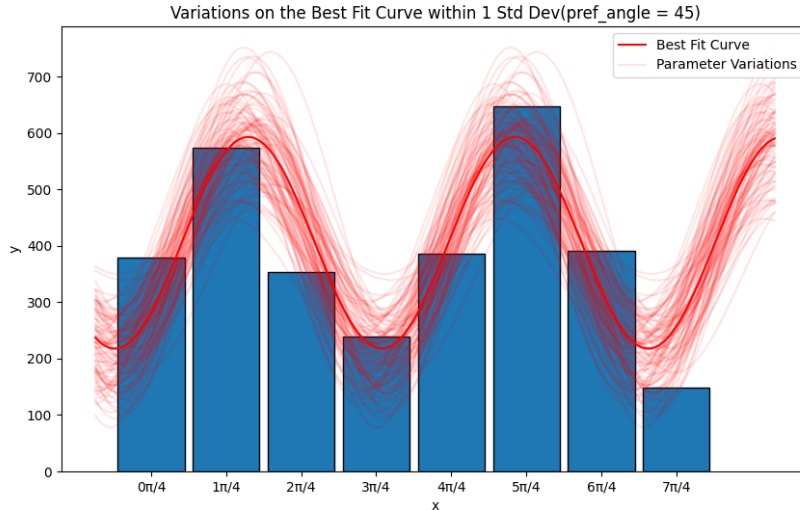


Figure 4.7: Results of curve fitting on X axis polarised

4.2.1 Oblique incidences

Studying oblique incidences is more important and more difficult than studying just normal incidence as most detected GRBs will be viewed significantly off-axis. The major problem that is posed by Compton Scattering in this arrangement is that there is a very significant chance that the scattered photon will either :

1. Get scattered with $\theta\pi/2$ and escape the 3x3 layer of pixels we are considering.
2. Get forward scattered and still end up in the ‘forward’ angular bin.

Both these effects end up meaning that there are very few counts in most of the angular bins hence the 300,000 photons I simulated for the previous normally incident mono-energetic simulations no-longer seem sufficient, regardless I will proceed with the same number of photons to demonstrate the results with uncertainties present in actual operations. Besides, the cosine form of the modulation curve does not strictly hold for off axis [1] incidences and thus the template matching method performs better the further away from the z axis we go.

As a side note, implementing polarisation angle dependent scattering was not a trivial task for the oblique incidence case as it involved rotating the direction of propagation based on the polarisation vector which unlike the normal incidence case did not have an easy definition. The implementation I ended up working with has the following idiosyncrasies:

1. Normal Incidence has been implemented as a special case of the oblique incidence case, one with incident θ and ϕ as zero each. Indeed keeping both of these as non-zero but small returns the results of the normal incidence discussed before.
2. I ask the user for the “preferred angle” which is used to generate the polarisation vector. The preferred angle defines a unit vector in the xy-plane, which is crossed with the incident direction and that defines a polarisation direction.

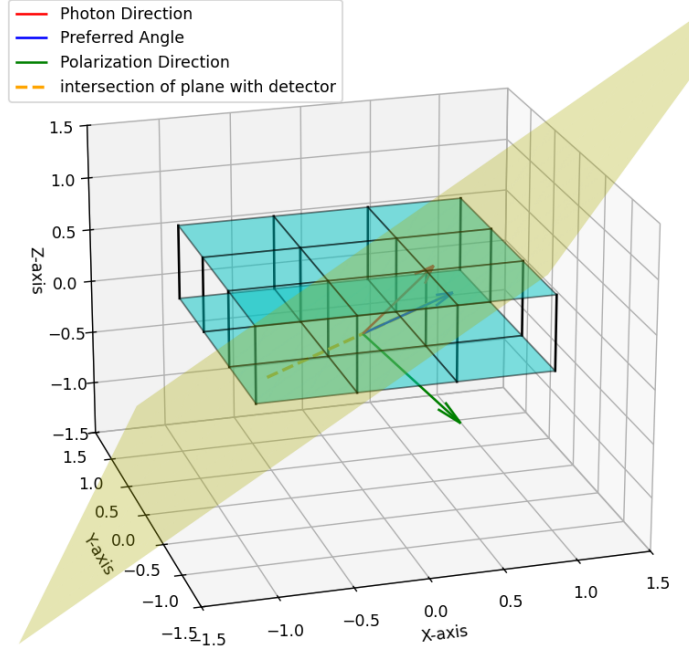


Figure 4.8: Geometry of the 3x3 detector

I have named the preferred angle as I have, because the nature of the KN cross section gives us the preferred scattering direction within the xy plane as that vector itself. The yellow plane is the perpendicular plane to the polarisation direction and the preferred angle lies in that plane. Eventually rotating the oblique propagation vector as a task required coding in the following 3D geometry (given in the figure below) and rotation matrices using the Rodrigues rotation matrix for rotations around an arbitrary axis.

Let the normalized rotation axis be represented as $\mathbf{u} = (x, y, z)$, and let the angle of rotation be θ . Define:

$$\cos(\theta) = c, \quad \sin(\theta) = s$$

The Rodrigues rotation matrix \mathbf{R}_θ based on this axis and angle is:

$$\mathbf{R} = \begin{bmatrix} c + x^2(1 - c) & xy(1 - c) - zs & xz(1 - c) + ys \\ yx(1 - c) + zs & c + y^2(1 - c) & yz(1 - c) - xs \\ zx(1 - c) - ys & zy(1 - c) + xs & c + z^2(1 - c) \end{bmatrix}$$

To implement scattering, the sampled values of θ and ϕ are used to create rotation matrices R_θ and R_ϕ . First we use R_θ to rotate the propagation vector along the common perpendicular which functioning like the y axis (shown in figure 4.8). Then we R_ϕ to rotate this intermediate vector around the propagation direction itself. This treatment ensures ϕ is measured assuming polarisation direction as the x axis. Here is a representative histogram of the simulations for the case where incidence has $\theta = \pi/6$ and $\phi = 0$ and the preferred angle as 0 radians.

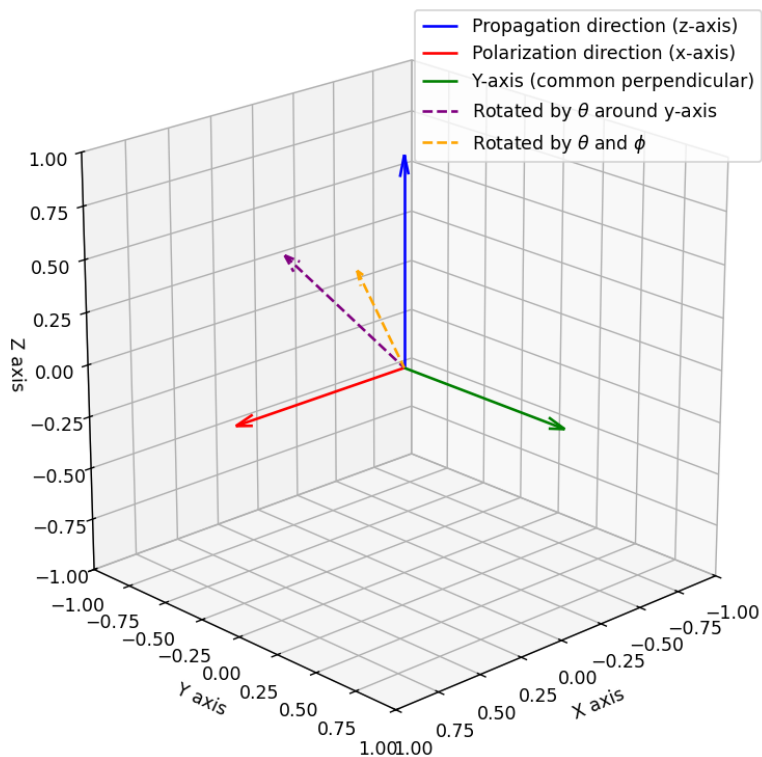


Figure 4.9: Vectors involved in rotation

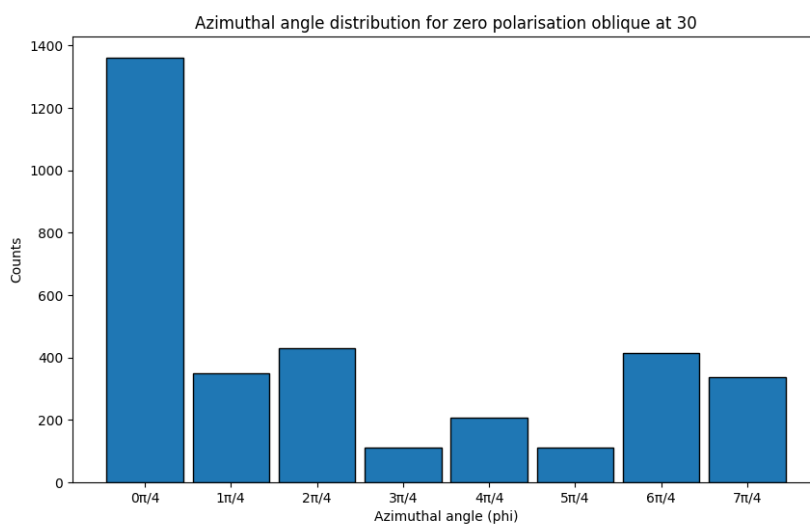


Figure 4.10: Scattering distribution for unpolarised 30 degree incidence

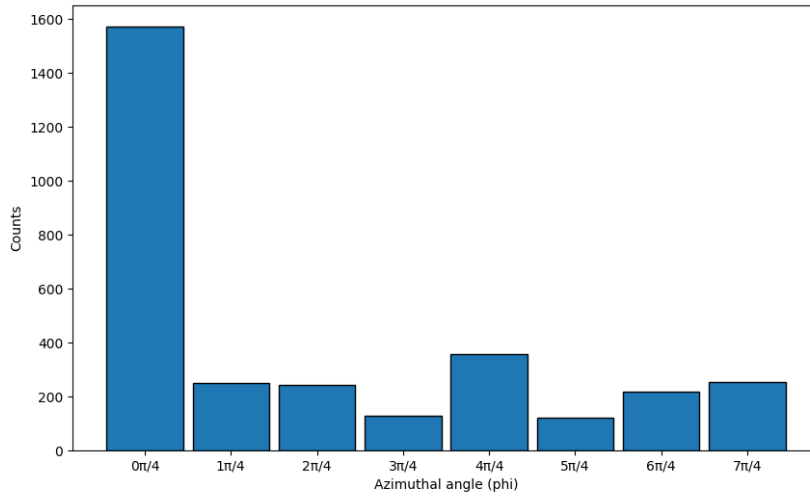


Figure 4.11: Distribution of 100% polarised fraction for oblique incidence

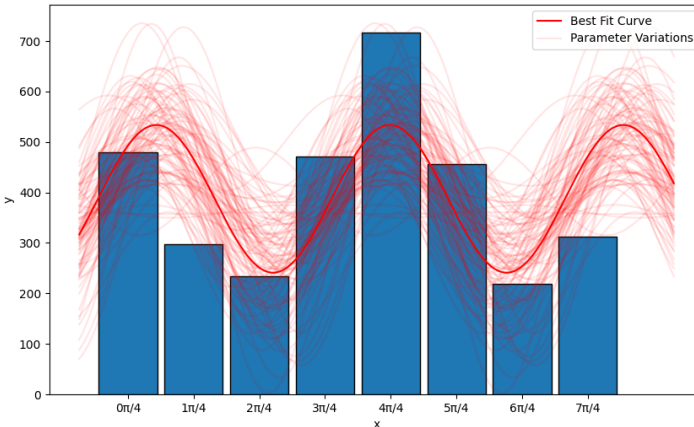


Figure 4.12: Overplotted variations of the best fit curve

The following should be noticed as unique about these simulations:

1. The vast majority of counts in the raw histogram tend to be in the 'zero' bin which is directly facing the incoming direction of the photon. This bin will move as we change ϕ , which was set to zero.
2. The counts in the other bins are quite a bit lower and will have variability from run to run. Which means it is more difficult to get secure polarisation measurements from these obliquely viewed GRBs.
3. The geometric correction when applied will still actually show a lack of counts due to most interactions scattered at 0 escaping the 3x3 grid.
4. The overplotted variations of the best fit curve will also tell us that the fit is not as secure.

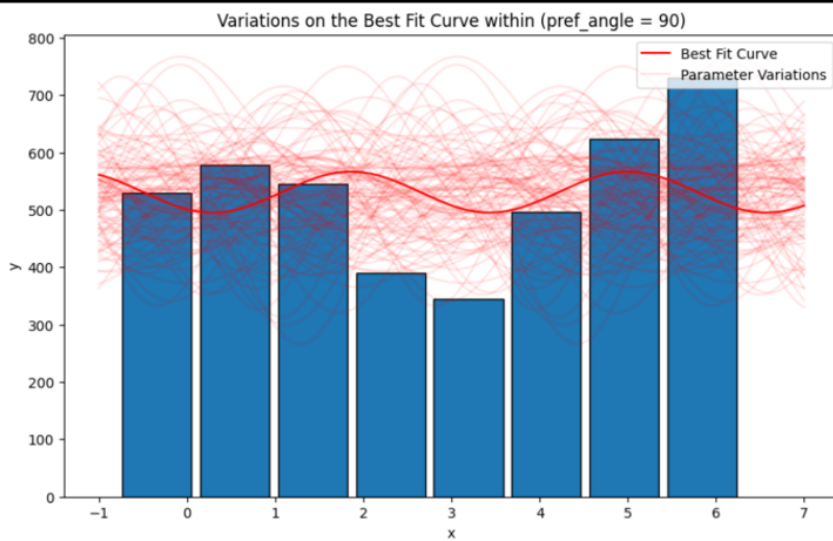


Figure 4.13: A simulation with $\theta = 45$

Eventually, the obtained parameters from the simulation of the detector and the cosine fitting have non-trivial idiosyncrasies at significantly oblique incidence angles. As I mentioned earlier this is confirmation of the fact that the cosine formula discussed up till now is not strictly applicable to significantly off-axis measurements. Thus to perform polarimetric measurements in real life, the template matching technique is the only option left which requires much more extensive simulation needs to be done for the actual instrument launched into space. The necessity of calibration is obvious since the PA and PF values assigned to a GRB are specific to that detector itself.

4.3 Daksha : Improving upon CZTI

The primary take away from the previous section's table is that the accuracy and precision of the recovered PA and PF goes down as the obliqueness increases and fundamentally this is due to the lack of valid Compton counts. Even in this idealised scenario where the interactions with other parts of the satellite need not be considered, the polarisation in the signature becomes much weaker. In real life, CZTI does not function as an all sky polarimeter, and can perform polarimetry for less than 60 degrees off axis incidence due to the lack of accurate mass models beyond that.

The in-development Daksha mission aims to be an all sky polarimeter [3] which is expected to give rise to 5 times the number of secure polarisation measurements per year that CZTI has produced [1] and it achieves that in the following ways:

1. Daksha has a symmetrical design, thus taking away the problem of off axis measurements to a great extent. Two identical satellites have been proposed, having the shape of a rhombicuboctahedron, which is a solid with eighteen square and eight equilateral triangle faces, and will approximate a hemisphere. Both satellites when launched in low-earth orbits on opposite sides of the Earth, combined end up giving us all sky coverage and hence sensitivity to more GRBs in the first place.
2. Calculations show that the minimum detectable polarisation (MDP) for Daksha is 30% for sources with fluence of 10^{-4} ergs per cm^2 . Which means that the PF

obtained from the degree of modulation has a less than 1% chance of being due to chance for detected polarisations above 30%. Thus if we assume GRBs are highly polarised then comparing with the Fermi GBM catalog [1] finds that Daksha will produce 5 times the secure polarisation measurements than CZTI has.

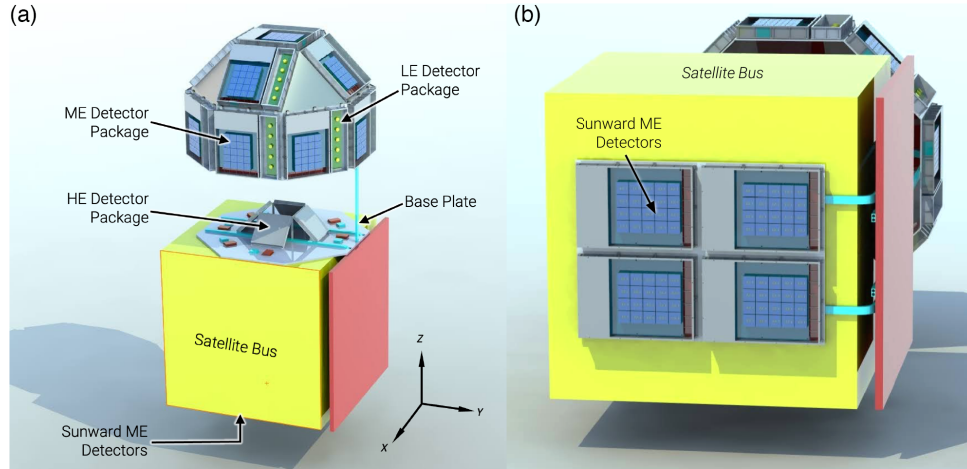


Figure 4.14: Schematic of Daksha

Chapter 5

Conclusion and Future work

As the results of the simulations presented in this chapter indicate, the rejection-sampling based Monte Carlo methods of describing interactions of high energy photons with a solid state pixelated detector is quite successful in replicating the kind of behaviour we would expect incoming photons undergoing Compton scattering to exhibit and moreover, the codes developed by myself can serve as a pedagogical tool for understanding the Compton effect, Klein-Nishina cross section and the Compton double-event based in-situ polarimetry used in present GRB polarimeters.

Clearly this kind of methodology, due to the rare nature of these double interactions, is extremely photon hungry and deviations from ideal viewing conditions (such as significantly off-axis incidence) pose a real challenge to the field that future missions such as Daksha and POLAR-2 will aim to overcome by developing more sensitive and dedicated polarimeters that are well-calibrated and characterised so as to allow for more frequent as well as secure linear polarisation measurements of GRB prompt emission. Daksha in specific is a symmetric instrument and the MDP values do not vary significantly with changing incidence angles.

Building catalogues of such measurements will ultimately allow experiments to catch up to the theoretical work already undertaken in calculating the polarisaed radiation from collimated jets and serve as a means to verify or rule out GRB prompt emission mechanisms based on the ensemble statistics.

5.1 Joint Polarisation Measurements

I am more than excited to be part of the first set of such joint analyses being done with co-detected GRBs from POLAR and CZTI. This particular joint-analysis takes on specific importance since in the catalogues published by both the science teams, different general conclusions were reached about the linear polarisation of GRBs. CZTI gave the impression that a good fraction of GRBs had a relatively high PF of around 50-60 % whereas POLAR's conclusions gave PF posteriors that peaked around 10-25%. However none of the GRBs published were common in between the two due to first of all a lack of co-detected GRBs, and secondly the few that existed not being analysed due to the lack of Compton counts in one or the other instrument. With the development of the new python package Polpy, which serves as a new plugin to the 3ML framework and the standardisation of the file formats of the outputs of the present and future polarimeters such as AstroSat-CZTI, Daksha, POLAR, POLAR-2, we are entering the era of many more co-detected GRBs and joint polarisation measurements and these efforts will serve as important cross-validations of the methodologies and instrumentations of the polarimeters involved as well as more secure PA and PF inferences that will help in confirming and

denying theoretical predictions about GRB prompt emission mechanisms.

5.2 10 year catalog of AstroSat CZTI

We are approaching 10 years of the CZTI being operational and detecting GRBs. The first CZTI 5-year catalogue paper was released in 2020, and now with the catalogue being updated with old data products reanalysed, we are in a position to finally make strong conclusions regarding the ensemble properties of the GRB population. This will involve much statistical and simulation work and I am eager to contribute and make this effort smoother and more successful.

5.3 Daksha : Next generation Polarisation mission

Much is to be said and has already been said in the papers published for the proposed Daksha mission in the way of its superior science capabilities. Indeed, its all-sky monitoring capabilities and resistance to earth occultation due to the presence of two satellites make it a much more sensitive polarimeter, and will probably lead to a step-jump in the rate of secure Polarisations acquired. The next generation polarimeters will help us hone in on the correct theories behind GRB prompt emission in an accelerated fashion.

Daksha will also advance science goals in the fields of EMGW multi-messenger astronomy, magnetars, active galactic nuclei and many more transient events due to its multitude of detectors on board.

5.4 Acknowledgments

I would like to thank Professor Varun Bhalerao for being a very helpful and illuminating guide for me on this and other projects I have undertaken with the STAR Lab so far, all of which in a way have contributed to my understanding of the field of GRBs and astrophysics in general. I would also like to thank Utkarsh Pathak from the STAR lab for sharing his understanding of the field with me and enabling me to dive deep into this topic with his constant inputs.

Bibliography

- [1] Suman Bala, Sujay Mate, Advait Mehla, Parth Sastry, N. P. S. Mithun, Sourav Palit, Mehul Vijay Chanda, Divita Saraogi, C. S. Vaishnava, Gaurav Waratkar, Varun Bhalerao, Dipankar Bhattacharya, Shriharsh Tendulkar, and Santosh Vadawale. Prospects of measuring gamma-ray burst polarization with the daksha mission. *Journal of Astronomical Telescopes, Instruments, and Systems*, 9(04), October 2023.
- [2] D. Band, J. Matteson, L. Ford, B. Schaefer, D. Palmer, B. Teegarden, T. Cline, M. Briggs, W. Paciesas, G. Pendleton, G. Fishman, C. Kouveliotou, C. Meegan, R. Wilson, and P. Lestrade. BATSE Observations of Gamma-Ray Burst Spectra. I. Spectral Diversity. , 413:281, August 1993.
- [3] Varun Bhalerao, Santosh Vadawale, Shriharsh Tendulkar, Dipankar Bhattacharya, Vikram Rana, Hitesh Kumar L. Adalja, Hrishikesh Belatikar, Mahesh Bhaganagare, Gulab Dewangan, Abhijeet Ghodgaonkar, Shiv Kumar Goyal, Suresh Gunasekaran, P J Guruprasad, Jayprakash G. Koyande, Salil Kulkarni, APK Kutty, Tinkal Ladiya, Deepak Marla, Sujay Mate, N. P. S. Mithun, Rakesh Mote, Sanjoli Narang, Ayush Nema, Sudhanshu Nimbalkar, Archana Pai, Sourav Palit, Arpit Patel, Jinaykumar Patel, Priya Pradeep, Prabhu Ramachandran, B. S. Bharath Saiguhan, Divita Saraogi, Disha Sawant, M. Shanmugam, Piyush Sharma, Amit Shetye, Shreeya Singh, Nishant Singh, Akshat Singhal, S. Sreekumar, Srividhya Sridhar, Rahul Srinivasan, Siddharth Tallur, Neeraj K. Tiwari, Amrutha Lakshmi Vadladi, C. S. Vaishnava, Sandeep Vishwakarma, and Gaurav Waratkar. Daksha: On alert for high energy transients, 2024.
- [4] T. Chattopadhyay, S. V. Vadawale, A. R. Rao, S. Sreekumar, and D. Bhattacharya. Prospects of hard X-ray polarimetry with Astrosat-CZTI. *Experimental Astronomy*, 37(3):555–577, November 2014.
- [5] Tanmoy Chattopadhyay, Soumya Gupta, Shabnam Iyyani, Divita Saraogi, Vidushi Sharma, Anastasia Tsvetkova, Ajay Ratheesh, Rahul Gupta, N. P. S. Mithun, C. S. Vaishnava, Vipul Prasad, E. Aarthy, Abhay Kumar, A. R. Rao, Santosh Vadawale, Varun Bhalerao, Dipankar Bhattacharya, Ajay Vibhute, and Dmitry Frederiks. Hard x-ray polarization catalog for a five-year sample of gamma-ray bursts using astrosat czt imager. *The Astrophysical Journal*, 936(1):12, August 2022.
- [6] Ramandeep Gill, Jonathan Granot, and Pawan Kumar. Linear polarization in gamma-ray burst prompt emission. *Monthly Notices of the Royal Astronomical Society*, 491(3):3343–3373, 10 2019.
- [7] Ramandeep Gill, Merlin Kole, and Jonathan Granot. Grb polarization: A unique probe of grb physics, 2021.

- [8] Glenn F. Knoll. *Radiation Detection and Measurement*, 3rd ed. John Wiley and Sons, New York, 3rd edition edition, 2000.
- [9] M. Kole, N. De Angelis, F. Berlato, J. M. Burgess, N. Gauvin, J. Greiner, W. Hajdas, H. C. Li, Z. H. Li, A. Pollo, N. Produit, D. Rybka, L. M. Song, J. C. Sun, J. Szabelski, T. Tymieniecka, Y. H. Wang, B. B. Wu, X. Wu, S. L. Xiong, S. N. Zhang, and Y. J. Zhang. The polar gamma-ray burst polarization catalog. *Astronomy and Astrophysics*, 644:A124, December 2020.
- [10] Merlin Kole and Jianchao Sun. *Gamma-Ray Polarimetry of Transient Sources with POLAR*, page 1–40. Springer Nature Singapore, 2022.
- [11] Andrew Levan, Paul Crowther, Richard de Grijs, Norbert Langer, Dong Xu, and Sung-Chul Yoon. Gamma-ray burst progenitors. *Space Science Reviews*, 202(1–4):33–78, November 2016.
- [12] Tsvi Piran. The physics of gamma-ray bursts. *Rev. Mod. Phys.*, 76:1143–1210, Jan 2005.
- [13] Vidushi Sharma, Shabnam Iyyani, Dipankar Bhattacharya, Tanmoy Chattopadhyay, A. R. Rao, E. Aarthy, Santosh V. Vadawale, N. P. S. Mithun, Varun. B. Bhalerao, Felix Ryde, and Asaf Pe'er. Time-varying polarized gamma-rays from grb 160821a: Evidence for ordered magnetic fields. *The Astrophysical Journal Letters*, 882(1):L10, September 2019.
- [14] Vidushi Sharma, Shabnam Iyyani, Dipankar Bhattacharya, Tanmoy Chattopadhyay, Santosh V Vadawale, and Varun B Bhalerao. Spectropolarimetric analysis of prompt emission of grb 160325a: jet with evolving environment of internal shocks. *Monthly Notices of the Royal Astronomical Society*, 493(4):5218–5232, March 2020.
- [15] Kenji Toma, Takanori Sakamoto, Bing Zhang, Joanne E. Hill, Mark L. McConnell, Peter F. Bloser, Ryo Yamazaki, Kunihito Ioka, and Takashi Nakamura. Statistical Properties of Gamma-Ray Burst Polarization. , 698(2):1042–1053, June 2009.
- [16] Vadawale, S. V., Chattopadhyay, T., Rao, A. R., Bhattacharya, D., Bhalerao, V. B., Vagshette, N., Pawar, P., and Sreekumar, S. Hard x-ray polarimetry with astrosat-czti. *AA*, 578:A73, 2015.
- [17] Maia A. Williams, Jamie A. Kennea, S. Dichiara, Kohei Kobayashi, Wataru B. Iwakiri, Andrew P. Beardmore, P. A. Evans, Sebastian Heinz, Amy Lien, S. R. Oates, Hitoshi Negoro, S. Bradley Cenko, Douglas J. K. Buisson, Dieter H. Hartmann, and Gaurava K. Jaisawal. Grb 221009a: Discovery of an exceptionally rare nearby and energetic gamma-ray burst. *The Astrophysical Journal Letters*, 946(1):L24, mar 2023.
- [18] Yuji YAZAKI. How the klein–nishina formula was derived: Based on the sangokan nishina source materials. *Proceedings of the Japan Academy, Series B*, 93(6):399–421, 2017.